

Micro Modeling of Solid Oxide Fuel Cell Anode based on Stochastic Reconstruction

Yoshinori Suzue^{1,2}, Naoki Shikazono¹ and Nobuhide Kasagi¹

¹Department of Mechanical Engineering, The University of Tokyo,
Hongo 7-3-1, Bunkyo-ku, Tokyo 113-8656, Japan

²Corresponding Author Present Address: Nakamachi 4-2-1-204, Machida, Tokyo 194-0021, Japan

E-mail address: suzue@thtlab.t.u-tokyo.ac.jp

Tel: +81-42-723-2989 Fax: +81-42-723-2989

ABSTRACT

A novel modeling scheme of SOFC anode based on the stochastic reconstruction technique and the Lattice Boltzmann method (LBM) is proposed and applied to the performance assessment and also to the optimization of anode microstructures. A cross-sectional microscopy image is exploited to obtain a two-dimensional phase map (*i.e.*, Ni, YSZ and pore), of which two-point correlation functions are used to reconstruct a three-dimensional model microstructure. Then, the polarization resistance of the reconstructed anode is obtained by the LBM simulation. The predicted anodic polarization resistance for a given microstructure and its sintering temperature dependence are in good agreement with the literature data. Three-dimensional distributions of potential and current can be obtained, while and the effect of working temperature is discussed. The proposed method is considered as a promising tool for designing SOFC anodes.

Key Words: Solid Oxide Fuel Cell, Electrode, Modeling, Stochastic Reconstruction, Lattice Boltzmann Method

1. Introduction

Solid oxide fuel cells (SOFCs) are considered to be one of the most powerful candidates for the future energy systems, because of their high efficiency and fuel flexibility [1]. In addition, their high temperature waste heat can be utilized in a heat engine, achieving an overall efficiency over 60 % [2], and also for fuel reforming. On the other hand, improved performance at lower temperature operation is desirable for cost reduction and system durability. Recently, anode-supported SOFCs with thin electrolyte have attracted interest [3], because their low ohmic loss enables lower temperature operation.

Generally, porous cermets (such as Ni-YSZ composite) are used as anode materials in order to match the thermal expansion coefficient with that of electrolyte and to extend effective reaction sites (three-phase boundary, TPB). Anode microstructure parameters (porosity, grain diameter, *etc.*) are known to have significant effects upon the cell performance and durability [4,5]. For the detailed evaluations of these parameters, numerical modeling of anode microstructures has been strongly demanded [6-10].

Conventional electrode modeling is mainly classified into three types, *i.e.*, (i) thin-film model (or pore model) [6], (ii) random resistor network model [7,8], and (iii) random packing sphere model [9,10]. In the first model, the network of ionic conductor is treated as tree-like protrusion covered with electronic conductors. In the second model, particles of ionic and electronic conductors are randomly distributed by a Monte Carlo technique, and modeled as a resistor network. Then, the overpotential in modeled electrode is obtained by solving Kirchoff's law in this resistor network. The third model is an advanced model of classical electrode models [11]: ionic and electronic conductivity and TPB density are calculated by applying the percolation theory [12] and the coordination number theory [13] of randomly packed spheres. Most of these models rely on the macroscopic homogeneity of composite electrode media, and their consistency with the actual electrode structures experimentally observed [14] has not been assured.

Recently, detailed microscopic (grain-scale) simulation of SOFC electrodes has been paid more attention [15,16]. Joshi *et al.* [15] performed detailed multi-component diffusion simulation, while Abbaspour *et al.* [16] solved the species-transport problem coupled with electrochemical reaction in

modeled electrodes. However, their electrode model is only two-dimensional being over-simplified as somewhat artificial configuration. Recently, Wilson *et al.* [17] performed the detailed measurement of 3D microstructure of anodes using FIB-SEM, and solved the mass transport in the measured microstructure by FEM. However it requires huge efforts for measurement and data processing, and the effect of microstructures upon electrochemical activity remains unclear.

Mukherjee and Wang [18] proposed a detailed modeling scheme of species and charge transport in a polymer electrolyte fuel cell (PEFC) catalyst layer. The realistic porous microstructure of the catalyst layer was reconstructed by using the stochastic reconstruction scheme originally proposed by Quiblier [19]. This modeling scheme could offer better understanding of PEFC microstructures and their effects upon cell performance. However, their catalyst layer model assumed only two phases, *i.e.*, gas phase and mixed electrolyte/electrode phase, and empirical Bruggeman correlation was employed for the solid phase conduction. In SOFC anodes, the ionic conductor (YSZ), the electronic conductor (Ni) and the gas phase conductor (pore) are comparable in size and volume fraction, so that such two-phase assumption cannot be readily verified.

In this study, anode microstructures are reconstructed by using the reconstruction scheme for multiphase media proposed by Yeong and Torquato [20]. Then, the anodic overpotential of the reconstructed structures is obtained by using the Lattice Boltzmann method (LBM) [21]. The effects of sintering temperature upon anode microstructures and cell performances are evaluated. Furthermore, the effects of working temperature on activation polarizations as well as on local three-dimensional distributions of potential and current are discussed.

2. Sample Preparation

Composite anode samples were prepared by mixing 8 mol% YSZ and nickel oxide (NiO) powders (AGC Seimi Chemical Co. Ltd., Japan, averaged grain diameter = 1.5 μm). Mixing ratio of NiO and YSZ was 60 : 40 wt%, and the Ni-YSZ volume ratio resulted as 42.4 : 57.6 after reduction. Samples were molded into rods by extrusion molding (Kankyo Ceramics Research Co. Ltd., Japan). Three sets of samples were pre-sintered at 1000 °C for 3 hours, and sintered for 3 hours. Sintering temperature was changed as 1300, 1350 or 1400 °C for evaluating the effects of sintering

temperatures. Then, sample anodes were reduced in 67 % H₂ diluted with N₂ at 750 °C for 10 hours. The ramp rate was 10 °C/min in all heating and cooling processes. A porosity of a 1200 °C-sintered sample was measured by a mercury porosimeter (Autopore IV9500, Shimadzu, Japan). The porosities of 1300, 1350 and 1400 °C-sintered samples extrapolated from their shrinkage ratios were 0.450, 0.393 and 0.335, respectively.

After reduction, samples were infiltrated with epoxy to avoid smearing of soft Ni, and polished with a diamond paste. For the stochastic reconstruction described later, highly flat cross-sectional surfaces should be obtained. In order to evaluate the surface roughness, cross-section of a polished sample is measured with a scanning probe microscope (SPM9600, Shimadzu, Japan; 512 × 512 pixels, dynamic mode AFM). As shown in Fig. 1, the surface roughness was less than 80 nm, and considered to be negligibly small compared to the grain size.

Cross-sectional optical images of polished samples were obtained with a confocal laser microscope (OLS3000, Shimadzu, Japan; 1024 pixel × 768 pixel, 1 pixel = 41 nm). The original microscopy images are shown in Fig. 2. Ni (white), YSZ (gray) and pore (black) can be clearly distinguished. Grain growth under high-temperature sintering was observed, especially for Ni.

3. Stochastic Reconstruction

3.1. 2D Image Processing

Three phases in raw images (Fig. 2) can be easily distinguished by their brightness values (see Fig. 3). To sharpen grain boundaries, a weighted differential filter was applied. Then, each phase was distinguished by applying the scheme of Lee *et al.* [22]. Threshold of brightness value was determined so that the volume fractions in the filtered image match with the values calculated from the porosity and the Ni-YSZ volume ratio. A phase-distinguished image of the 1400 °C-sintered sample is shown in Fig. 4, where clear phase differentiation is observed.

3.2. 2D Image Analysis

From the phase-distinguished 2D images, a phase function, $Z(\mathbf{x})$, is defined at each pixel (\mathbf{x}) as follows:

$$Z(\mathbf{x}) = \begin{cases} 0 & (\text{for } \mathbf{x} \in \text{pore, black}) \\ 1 & (\text{for } \mathbf{x} \in \text{YSZ, gray}) \\ 2 & (\text{for } \mathbf{x} \in \text{Ni, white}) \end{cases} \quad (1)$$

Using this phase function, the two-point correlation (or *probability*) function R_{ij} between phases i and j ($i, j = 0 - 2$) is defined as follows:

$$R_{ij}(r) = \frac{\overline{\delta(Z(\mathbf{x}), i) \delta(Z(\mathbf{x} + \mathbf{r}), j)}}{\overline{\delta(Z(\mathbf{x}), i)}}, \quad (2)$$

where $\delta(i, j)$ represents the Kronecker's delta function. Figure 5 shows the two-point correlation of Ni-Ni and YSZ-YSZ. These correlation functions did not fully converge on volume fractions due to insufficient imaging areas, but the error was relatively small (less than 5 %). As shown in Fig. 5, the YSZ-YSZ correlation seems to be more uniform than that of Ni-Ni, and this represents that YSZ grains are better dispersed in cermet anodes.

3.3. Stochastic Reconstruction

Stochastic reconstruction was originally proposed by Joshi *et al.* [23], and later extended into three-dimensions by Quiblier [19]. However, their schemes based on the Gaussian filtering are relatively poor in accuracy, and also not suitable for multiphase media. Therefore, the iterative scheme of Yeong and Torquato [20] is applied in this study. The grid length Δx is 0.178 μm in each direction, which is around 1/10 of the averaged grain diameter. This grid size is considered to be small enough from our preliminary calculation. The whole computational domain size is 150 grids (26.7 μm in space) cubic, and considered to be thick enough compared to the effective anode thickness ($\sim 20 \mu\text{m}$) [24]. Periodic boundary conditions are imposed in each direction. At first, each voxel is assigned randomly with three phases according to their volume fractions. Then, reconstruction is carried out to minimize the cost function E defined as follows:

$$E = \sum_{i,j} \int_0^{r_0} \{R_{ij}^{3D}(r) - R_{ij}^{2D}(r)\}^2 dr, \quad (3)$$

where R_{ij}^{3D} and R_{ij}^{2D} are the reconstructed and the original 2D two point correlation functions, respectively. Isotropic porous media are assumed, and the integral dr is performed only in the directions of the principal axes in order to reduce the computational load. The interval of integration r_0 was set as $7 \mu\text{m}$.

Starting from a random configuration, two voxels of different phases are exchanged at each iteration step only when the cost function E decreases. The reconstruction is terminated after the cost function remained constant for 50 Monte Carlo steps. Then, resulted porous structures are modified by using the surface curvature modification scheme [25] in order to avoid physically impossible structures such as “solid phase floating in a pore.”

3.4. Validity of Reconstructed Structure

Reconstructed 3D microstructures of three samples are shown in Fig. 6. Note that, in the figures, small parts of reconstructed structures (100 grid cubic) are smoothed out for eye-friendliness. Good agreement is achieved between reconstructed and original two-point correlation functions as shown in Fig. 7(a), with the residuals of Eq.(3) being less than 1.0 %,. In order to check the validity of the reconstructed structures, the lineal-path function $L_i(r)$ of the reconstructed structure is compared with that of the original 2D images.

$$L_i(r) = \frac{l_i(r)}{N_{\text{pixel}}}. \quad (4)$$

In Eq. (4), $l_i(r)$ represents the number of line segments of length r lying in phase i , while N_{pixel} represents the number of total pixels. As shown in Fig. 7(b), reconstructed lineal-path functions match well with those of the original 2D image.

4. Electrode Performance Simulation Scheme

4.1. Simulation Model

The anodic overpotential of reconstructed anodes is calculated from detailed numerical

simulations. A schematic of computational domain is shown in Fig. 8. In order to model the actual anode operating condition, current collector (CC) and YSZ electrolyte (EL) layers are added to the boundaries at $x = 0 \mu\text{m}$ and $x = 26.7 \mu\text{m}$ ($150\Delta x$), respectively. The thicknesses of the CC and the EL layers are $1.78 \mu\text{m}$ ($10\Delta x$) and $3.56 \mu\text{m}$ ($20\Delta x$), respectively. For simplicity, binary gas composition of $\text{H}_2/\text{H}_2\text{O}$ is assumed, and equimolar diffusion assumption [26] is employed,

$$D = \frac{p_{\text{H}_2\text{O}}}{p} D_{\text{H}_2} + \frac{p_{\text{H}_2}}{p} D_{\text{H}_2\text{O}}. \quad (5)$$

The diffusion coefficient of each species i is determined as:

$$D_i = \left(\frac{1}{D_{im}} + \frac{1}{D_{ik}} \right)^{-1}. \quad (6)$$

In Eq. (6), D_{im} and D_{ik} represent binary and Knudsen diffusion coefficients, respectively being given as:

$$D_{im} = 5.956 \times 10^{-4} \left(\frac{1}{M_{\text{H}_2}} + \frac{1}{M_{\text{H}_2\text{O}}} \right)^{1/2} \frac{T^{3/2}}{p \zeta^2 \Omega_D}, \quad (7)$$

$$D_{ik} = \frac{2}{3} \left(\frac{8RT}{\pi M_i} \right)^{1/2} r_p. \quad (8)$$

Gas properties are summarized in Table 1, and the collision integral Ω_D is represented as:

$$\Omega_D = 1.1336 (Tk / \varepsilon)^{-0.1814}. \quad (9)$$

The r_p in Eq. (8) represents the mean pore radius, and was set as $0.75 \mu\text{m}$ for all simulated cases.

Temperature is considered to be uniform, and uniform current is assumed at $x = -1.78\mu\text{m}$ ($-10\Delta x$) and $x = 30.26\mu\text{m}$ ($170\Delta x$). The material properties [27,28] are summarized in Table 1.

4.2. Governing Equations

The governing equations in the pore, Ni and YSZ phases are given as the diffusion equation of hydrogen gas and the charge transfer equations for electron and ion, respectively. They are written as follows:

$$\nabla(D\nabla C) = -\frac{i_{\text{react}}}{2F}, \quad (10)$$

$$\nabla(\sigma_{\text{elec}} \nabla \phi_{\text{elec}}) = -i_{\text{react}}, \quad (11)$$

$$\nabla(\sigma_{\text{ion}} \nabla \phi_{\text{ion}}) = i_{\text{react}}. \quad (12)$$

The RHSs in Eqs. (10)–(12) are the reaction production terms, and the local reaction current i_{react} is calculated by using the Butler-Volmer equation [29]:

$$i_{\text{react}} = i_0 L_{\text{TPB}} \left[\exp\left(\frac{2F}{RT} \eta\right) - \exp\left(-\frac{F}{RT} \eta\right) \right], \quad (13)$$

where η is the overpotential $\phi_{\text{elec}} - \phi_{\text{ion}}$. The lineal exchange current density i_0 is defined from the porous Ni anode experiments of de Boer [30] as:

$$i_0 = 31.4 \times p_{\text{H}_2}^{-0.03} p_{\text{H}_2\text{O}}^{0.40} \exp\left(-\frac{1.83 \times 10^4}{T}\right). \quad (14)$$

The three-phase boundary length per unit volume, L_{TPB} , in Eq. (13) is assumed to be 20 % smaller than the value directly calculated from the cubic voxel perimeter of the reconstructed structure. Geometrically, the actual TPB length should lie between 57.7-100 % of the cubic voxel perimeter. In the present study, the voxel perimeter was simply reduced by 20 % as a representative.

4.3. Numerical Scheme

The LBM is used to solve Eqs. (10)-(12) in each phase. The LB equation with the LBGK model in the collision term is written as follows:

$$f_i(\mathbf{x} + \mathbf{c}_i \Delta t, t + \Delta t) = f_i(\mathbf{x}, t) - \frac{1}{t^*} [f_i(\mathbf{x}, t) - f_i^{eq}(\mathbf{x}, t)] + w_i \Delta t \quad (15)$$

In Eq. (15), f_i represents the velocity distribution function of gas, electron or ion with velocity \mathbf{c}_i in the i th direction, and f_i^{eq} is the Maxwellian local equilibrium distribution. For the 3D LBM simulation, D3Q15 ($i = 1-15$) or D3Q19 ($i = 1-19$) models are commonly used. However, it has been shown that, in case of simple diffusion simulation, D3Q6 ($i = 1-6$) model can be used with a slight loss of accuracy [31]. So the D3Q6 model is used in this work. The relaxation time t^* is 0.99 and fixed for all simulations.

Periodic boundary conditions are assumed in the spanwise (y and z) directions. At the CC surface, constant gas composition is assumed. Constant electronic and ionic current flux conditions are imposed on the CC and EL boundaries. A no-flux boundary condition is imposed on the boundary of each phase in the porous media by applying the halfway bounceback scheme with second-order accuracy [32].

The production term w_i in the RHS is calculated from Eqs. (10)-(14) using a scheme similar to that of Mukherjee and Wang [18]. A schematic of reaction calculation is shown in Fig. 9. The reaction current at TPB ($i+1/2, j+1/2, k$) is calculated as:

$$i_{\text{reac}}(i + \frac{1}{2}, j + \frac{1}{2}, k) = i_0 \times L_{\text{TPB}}(i + \frac{1}{2}, j + \frac{1}{2}, k) \times \left\{ \exp\left(\frac{2F}{RT} \eta\right) - \exp\left(-\frac{F}{RT} \eta\right) \right\} / \Delta x^3 \quad (16)$$

$$\eta = \phi_{\text{elec}}(i, j, k) - \phi_{\text{ion}}(i + 1, j, k). \quad (17)$$

5. Computational Results

5.1. Electrode Performance

The calculated electronic and ionic conductivities, σ_{elec}^{eff} and σ_{ion}^{eff} , and gas phase tortuosity factor, τ , are shown in Fig. 10. With increasing the sintering temperature, the solid phase conductivities are improved while gas phase connectivity is reduced. The calculated gas phase tortuosity factors are in good agreement with the literature data ($\tau=2.5 - 4.0$) [33].

The reconstructed anode performances are compared with the experimental data [34]. The simulation conditions are summarized in Table 2. Since the experimental data was taken from the electrochemical impedance spectroscopy under zero bias current, only a small value of current $i=1 \times 10^{-4}$ A/cm² was assumed in this case. The temperature dependence of the anodic polarization resistance is shown in Fig. 11. It is found that the best anode performance is achieved by the sample sintered at 1400 °C. This tendency is in good agreement with the experimental results in literatures [34-35], especially with the results of Primdahl *et al.* [34], whose sample condition is similar to the present case.

This sintering temperature dependence can be explained by Thiele modulus Γ (effectiveness criterion) [36], which can be obtained by linearizing and coupling Eqs. (11)-(13):

$$\Gamma^2 = \frac{3i_0 L_{TPB} F (\rho_{ion}^{eff} + \rho_{elec}^{eff})}{RT} L^2. \quad (18)$$

Thiele modulus represents the ratio of ohmic resistance to the activation overpotential. Generally, ohmic resistance becomes dominant and reactive electrode thickness becomes inversely proportional to Γ when $\Gamma > 3$ [36]. For such cases, the order of the anode polarization loss can be expressed as:

$$\eta \propto \Gamma / L_{TPB} i_0 \propto \sqrt{\rho_{ion}^{eff} / L_{TPB} i_0}. \quad (19)$$

In Eq. (19), electronic resistivity is neglected because it is much smaller than the ionic resistivity.

In Fig. 12, the sintering temperature dependence of Thiele modulus Γ is shown. Thiele modulus Γ of each sample is larger than 3, and thus ohmic (ionic) resistance is dominant. Equation (19) reveals

that the anode polarization loss is dependent on the ionic resistivity ρ_{ion}^{eff} and the TPB density L_{TPB} . The calculated ionic resistivity and the TPB densities (L_{TPB}) are shown in Fig. 13. With increasing the sintering temperature, the ionic resistivity decreases while the TPB density increases, which leads to smaller polarization loss.

Also, the TPB densities in the modeled anodes are found to be around 2.4 - 2.8 μm^{-2} . This predicted TPB densities are somewhat smaller than the value obtained from FIB-SEM measurement 4.28 μm^{-2} [37]. However, the order of magnitude is the same although they are obtained from different samples.

5.2. Local Potential and Current Distributions

The effects of working temperature on local distributions of potential and current are investigated. Simulation conditions are summarized in Table 3. In order to investigate a high power density operating condition, the current density is set as $i=1 \text{ A/cm}^2$. In Fig. 14, the phase, current and potential distributions in an anode-electrolyte interface at $x = 26.7\mu\text{m}$ ($150\Delta x$) of the 1400 °C-sintered sample are shown. The y - z plane is in contact with the electrolyte (YSZ) surface, and thus the pore-Ni interfaces (red lines) represent TPBs. As shown in Fig. 14, the potential and current distributions are considerably inhomogeneous.

The predicted current distributions for different working temperatures are shown in Fig. 15. With decreasing the working temperature, the current density around TPBs is significantly increased (see Fig. 14(a)). In Fig. 16, the ionic current density distribution in the x direction is shown. Under 600 °C operation, the reactive electrode thickness becomes very thin ($< 5 \mu\text{m}$), and this fact means that the reaction is confined in this thin region due to relatively large ionic resistivity. Thus, the ionic current flows mainly in the vicinity of TPB. Even though Thiele modulus Γ decreases with the operating temperature as shown in Fig. 17, non-linear dependence of activation overpotential on current makes the ionic resistance dominant for this low temperature and large current density condition. In other words, the linearized Butler-Volmer equation in Thiele modulus Γ becomes invalid because exchange current density i_0 becomes small for such conditions. In the case of 600 °C operation, the activation resistance calculated from Eq. (13) is much smaller than the ionic resistivity,

making the reactive anode thickness quite thin.

Conclusions

A novel modeling scheme of SOFC anodes based on the stochastic 3D structure reconstruction scheme and the LBM simulation is proposed and evaluated for the prediction of the effects of anode microstructures on the total anode performance. Cross-sectional 2D microscopy images of anodes are processed to obtain phase-distinguished images, and 3D anode microstructure models are reconstructed from the two-point correlation functions of the 2D images. Good reconstruction is achieved by the present scheme, and residuals in two-point correlation functions and lineal-path functions are negligibly small.

The anodic overpotential of reconstructed anodes is calculated by coupling the mass and charge transfer and the electrochemical reaction using LBM, and the effect of anode microstructures on the cell performance is discussed. It is found that the optimal sintering temperature should be around 1400 °C, where a good ionic network and electrochemical activity are obtained. This result is in good agreement with the existing literature data.

By using this scheme, three-dimensional distributions of current and potential are obtained, and the effects of working temperature on local potential and current distributions are discussed. With the decrease of working temperature, the current concentrates near TPB of anode/electrolyte interface and the reactive anode thickness becomes thinner ($< 5 \mu\text{m}$). This is attributed to the dominance of ionic resistance over activation overpotential.

This scheme gives light to better understanding of microscale phenomena and the optimal design of microstructures in SOFC anodes.

The present scheme requires validation with the directly measured 3D data, such as FIB-SEM measurement in Ref. [17]. And this remains as a future challenge.

Acknowledgements

This research was supported through the 21st Century COE Program, “Mechanical System Innovation,” by the Ministry of Education, Culture, Sports, Science and Technology of Japan (MEXT). We would like to thank Prof. Yuji Suzuki at the University of Tokyo and Prof. Koji

Fukagata at Keio University for their advice and discussion. The authors also would like to thank Messrs. Yu Yamaguchi and Yusuke Sakamoto at the University of Tokyo for their cooperation in sample preparation and data acquisition.

- [1] SC. Singhal and K. Kendall, *High Temperature Solid Oxide Fuel Cells*, Elsevier (2002).
- [2] H. Uechi *et al.*, *ASME J. Eng. Gas Turbines and Power*, 126 (2004) 755.
- [3] SH. Chan *et al.*, *J. Power Sources*, 93 (2001) 130.
- [4] H. Abe *et al.*, *Thin Solid Films*, 496 (2006) 49.
- [5] H. Koide *et al.*, *Solid State Ionics*, 132 (2000) 253.
- [6] T. Kenjo *et al.*, *J. Electrochem. Soc.*, 138 (2) (1991) 349.
- [7] S. Sunde, *J. Electrochem. Soc.*, 143 (1996) 1930.
- [8] LCD. Schneider *et al.*, *Electrochimica Acta*, 52 (1) (2006) 314.
- [9] P. Costamagna *et al.*, *Electrochimica Acta*, 43 (1998) 375.
- [10] JH. Nam and DH. Jeon, *Electrochimica Acta*, 51 (2006) 3446.
- [11] M. Paulin *et al.*, *J. Electrochem. Soc.*, 124 (2) (1977), 180.
- [12] D. Stauffer, *Introduction to Percolation Theory*, Taylor & Francis (1995).
- [13] D. Bouvard and FF. Lange, *Acta Metall. Mater.*, 39 (12) (1991) 3083.
- [14] JH. Lee *et al.*, *Solid State Ionics*, 148 (2002) 15.
- [15] AS. Joshi, *J. Power Sources*, 164 (2007) 631.
- [16] A. Abbaspour *et al.*, *J. Power Sources*, 161 (2006) 965.
- [17] JR Wilson *et al.*, *Nature Materials*, 5 (2006) 541.
- [18] PP. Mukherjee and CY. Wang, *J. Electrochem Soc.*, 153 (2006) A840.
- [19] JA. Quiblier, *J. Colloid and Interface Sci.*, 98 (1984) 84.
- [20] CLY. Yeong and S. Torquato, *Phys. Rev. E.*, 58 (1998) 224.
- [21] S. Chen and GD. Doolen, *Annu. Rev. Fluid Mech.*, 30 (1998) 329.
- [22] KR. Lee *et al.*, *J. Power Sources*, 140 (2005) 226.
- [23] M. Joshi, Ph. D. Dissertation, University of Kansas, Lawrence, KS (1974).
- [24] H. Fukunaga *et al.*, *Electrochem. Solid-State Lett.*, 10 (1) (2007) B16.
- [25] DP. Bentz and NS. Martys, *Transport in Porous Media*, 17 (1994) 221.
- [26] SH. Chan and ZT. Xia, *J. Electrochem Soc.*, 148 (2001) A388.
- [27] U. Anselmi-Tamburini *et al.*, *Solid State Ionics*, 110 (1998) 35.
- [28] JR. Ferguson *et al.*, *J. Power Sources*, 110 (2002) 91.

- [29] T. Kawada *et al.*, *J. Electrochem Soc.*, 137 (1990) 3042.
- [30] B. De Boer, Ph. D. thesis, Univ. of Twente, The Netherland (1998).
- [31] T.H. Zeiser *et al.*, *Chem. Eng. Sci.*, 56 (2001) 1697.
- [32] M.A. Gallivan *et al.*, *Int. J. for Numerical Methods in Fluids*, 25 (1997) 249.
- [33] R.E. Williford *et al.*, *J. Electrochem. Soc.*, 150 (2003), A1067.
- [34] S. Primdahl *et al.*, *J. Am. Ceram. Soc.*, 83 (2000) 489.
- [35] S.P. Jiang, *J. Electrochem. Soc.*, 150 (2003) E548.
- [36] P. Costamagna *et al.*, *Electrochimica Acta*, 43 (1998) 967.
- [37] S. Barnet *et al.*, *Microsc. Microanal.*, 13 (2) (2007) 596.

Nomenclature

C	molar density [mol/m ³]
D	diffusion coefficient [m ² /s]
E	cost function of reconstruction
f_i	velocity distribution function
f_i^{eq}	equilibrium velocity distribution function
i	current density [A/m ²]
i_0	exchange current density per TPB length [A/m]
i_{reac}	reaction current density [A/m ³]
L	electrode thickness [μm]
$L_i(r)$	Lineal-path function
$l(r)$	number of line elements
L_{TPB}	TPB density per unit volume [m ⁻²]
N_{pixel}	number of pixels
p	pressure [Pa]
$R_{ij}(r)$	two-point correlation function
t^*	relaxation time
w_i	reaction production
$Z(\mathbf{x})$	phase function

Greek Symbols

ε	volume fraction
ϕ	potential [V]
Γ	Thiele modulus
η	over voltage [V]
ρ	resistivity [Ωm]
σ	conductivity [Sm ⁻¹]
τ	tortuosity factor

Subscripts & Superscripts

eff	effective value in porous media
elec	electron
ion	ion
H ₂	hydrogen
H ₂ O	vapor

List of Figures

- Fig. 1 Height image of a 1400 °C-sintered sample measured by a scanning probe microscope.
- Fig. 2 Original cross-sectional images of sample anodes sintered at (a) 1300 °C, (b) 1350 °C and (c) 1400 °C.
- Fig. 3 Brightness histogram of a 1400 °C-sintered sample.
- Fig. 4 Phase-distinguished image of a 1400 °C-sintered sample (Ni: white, YSZ: gray, pore: black).
- Fig. 5 Temperature dependence of two-point correlation functions of (a) Ni-Ni and (b) YSZ-YSZ.
- Fig. 6 Reconstructed anode microstructures sintered at (a) 1300 °C, (b) 1350 °C and (c) 1400 °C. Green: Ni, blue: YSZ, transparent gray: pore.
- Fig. 7 (a) Two-point correlation functions and (b) lineal-path functions of original 2D image and reconstructed 3D structure (1400 °C-sintered sample).
- Fig. 8 Schematic of a computational domain.
- Fig. 9 Schematic of reaction production at TPB.
- Fig. 10 (a) Conductivity of solid phases and (b) tortuosity factor of gas phase.
- Fig. 11 Effect of sintering temperature upon the anodic polarization resistance (comparison with literature data).
- Fig. 12 Sintering temperature dependence of the Thiele modulus Γ .
- Fig. 13 Sintering temperature dependence of the TPB density and the ionic resistance.
- Fig. 14 (a) Phase, (b) potential and (c) current distribution at anode-electrolyte interface of a 1400 °C-sintered sample. Phases in (a) are; white: Ni, light gray: YSZ, dark gray: pore, black: disconnected phases, red lines: TPB.
- Fig. 15 Temperature dependence of ionic current distribution at anode-electrolyte interface; (a) 600 C°, (b) 800 C° and (c) 1000 C°.
- Fig. 16 Effect of working temperature upon the effective anode thickness.
- Fig. 17 Working temperature dependence of the anodic overpotential and Thiele modulus Γ .

Table 1. Material properties used in simulation.

Properties	Value or expression
Electronic conductivity σ_{elec} [Sm^{-1}] ⁽²⁷⁾	$3.37 \times 10^6 - 1065.3T$
Ionic conductivity σ_{ion} [Sm^{-1}] ⁽²⁸⁾	$3.34 \times 10^4 \exp\left(-\frac{10300}{T}\right)$

Substance	M [10^{-3} kg/mol]	ζ [\AA]	ϵ/k [K]
H ₂	2.016	2.93	37
H ₂ O	18.015	2.65	356

Table 2. Simulation conditions in Sec. 5.1.

Properties	Value or expression
Operating temperature T [$^{\circ}\text{C}$]	1000
Pressure p [Pa]	1.013×10^5
Fuel composition (H ₂ :H ₂ O) [mol%]	97:3
Current density i [A/cm^2]	1.0×10^{-4}

Table 3. Simulation conditions in Sec. 5.2.

Properties	Value or expression
Pressure p [Pa]	1.013×10^5
Fuel composition (H ₂ :H ₂ O) [mol%]	80:20
Current density i [A/cm^2]	1.0

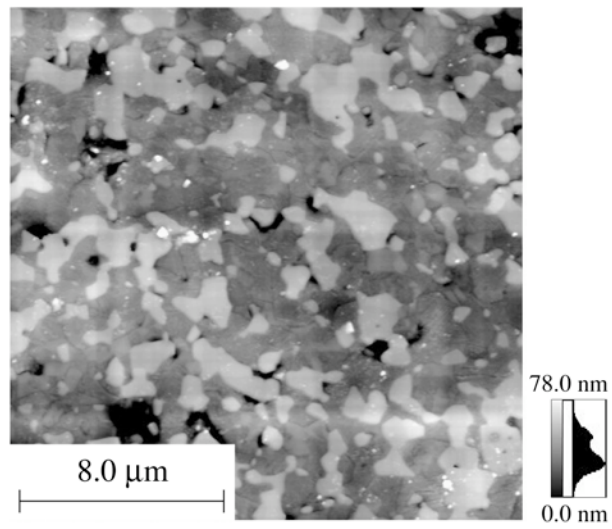


Fig.1

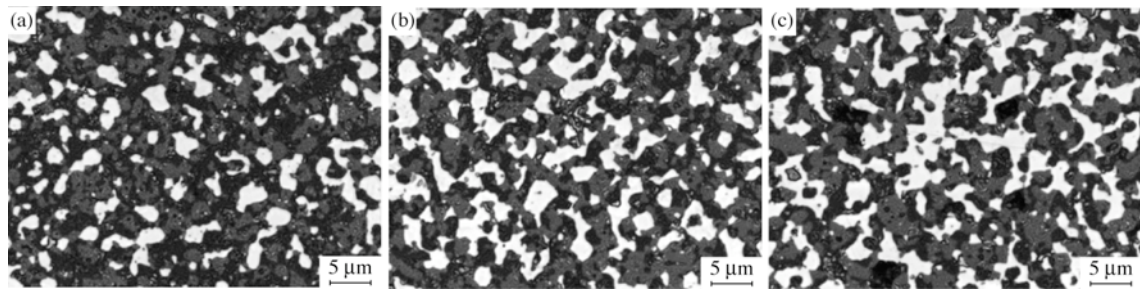


Fig. 2

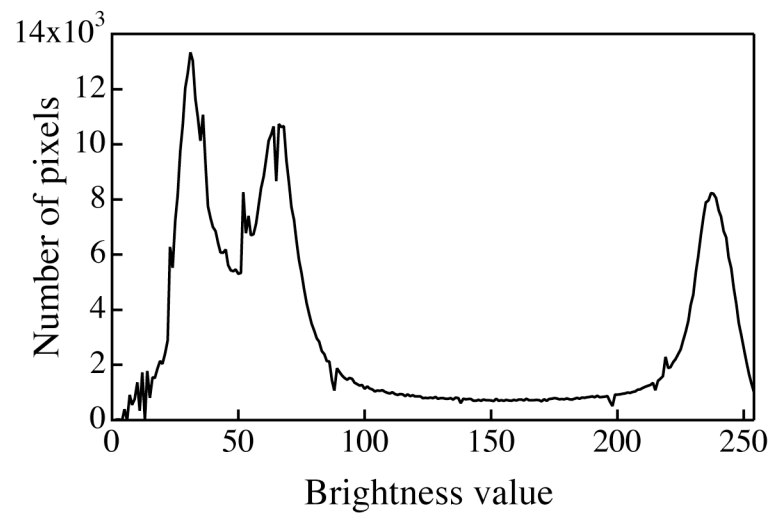


Fig. 3

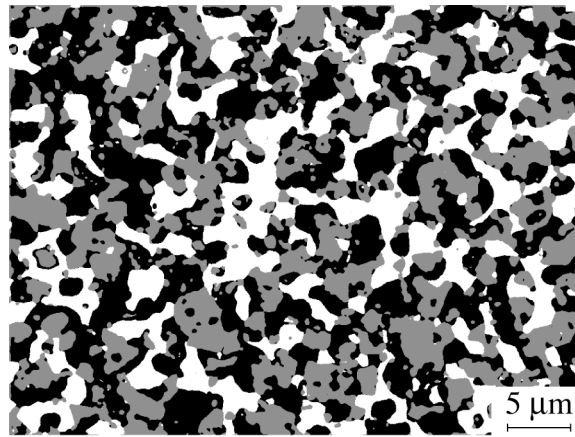


Fig. 4

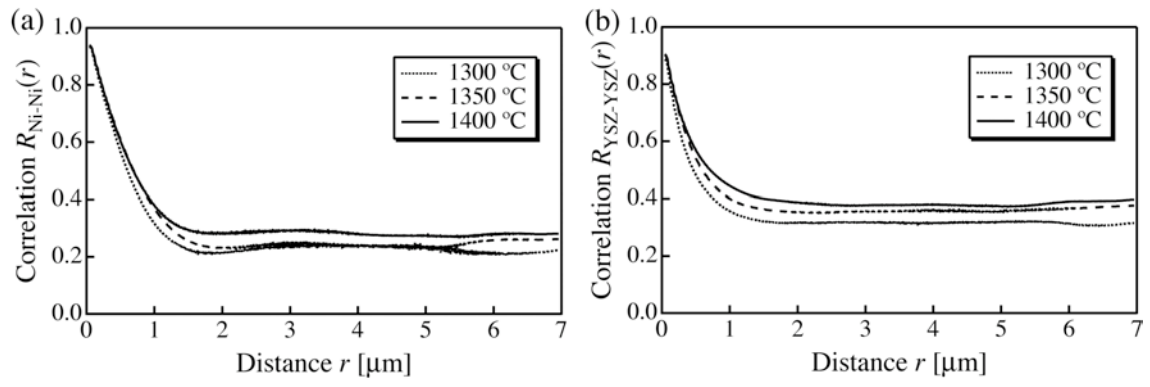


Fig. 5

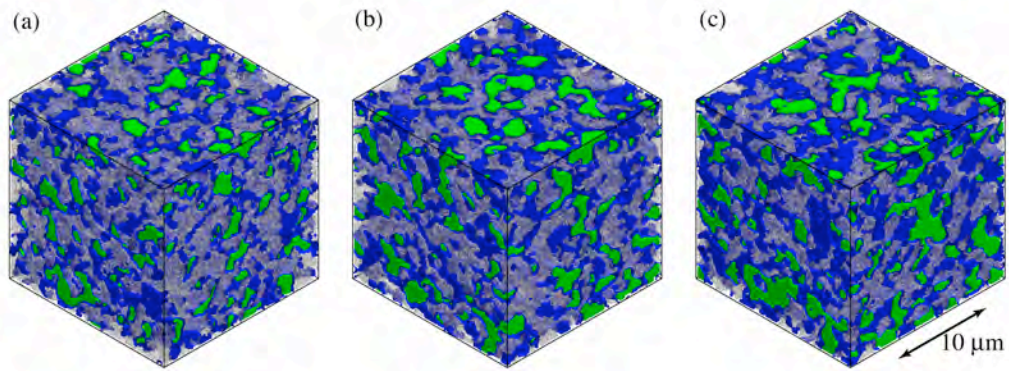


Fig. 6

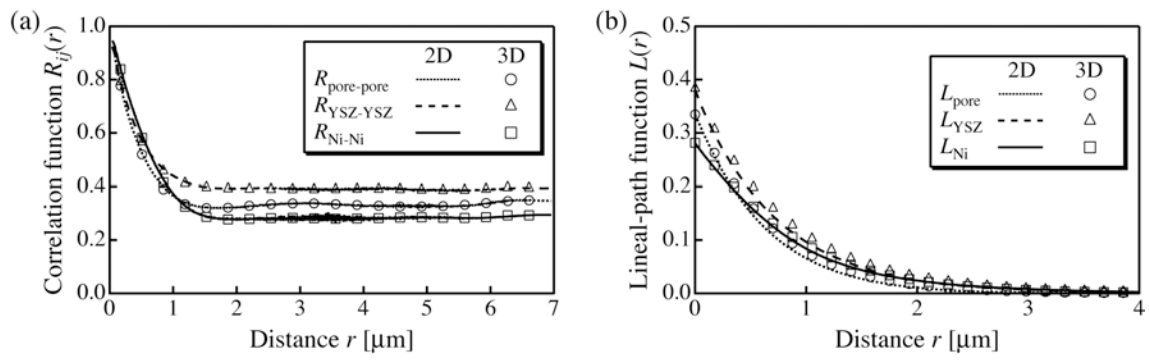


Fig. 7

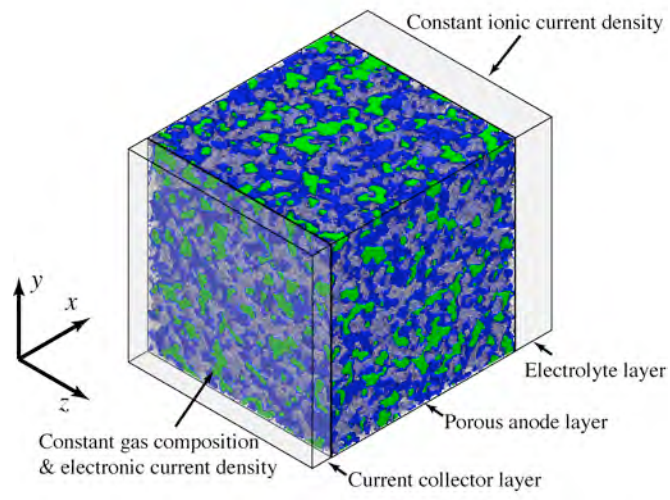


Fig. 8

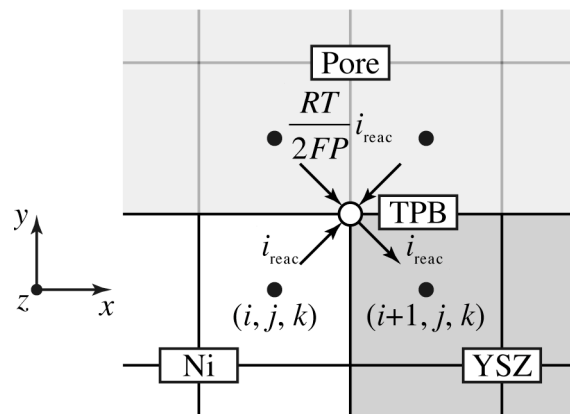


Fig. 9

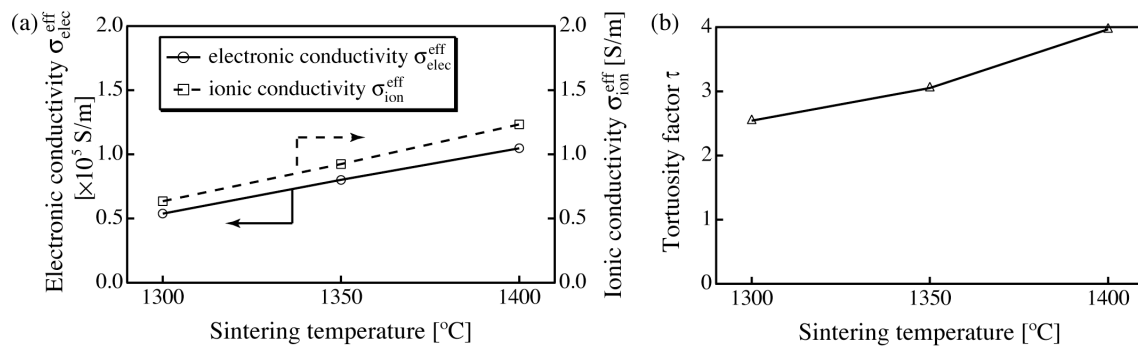


Fig. 10

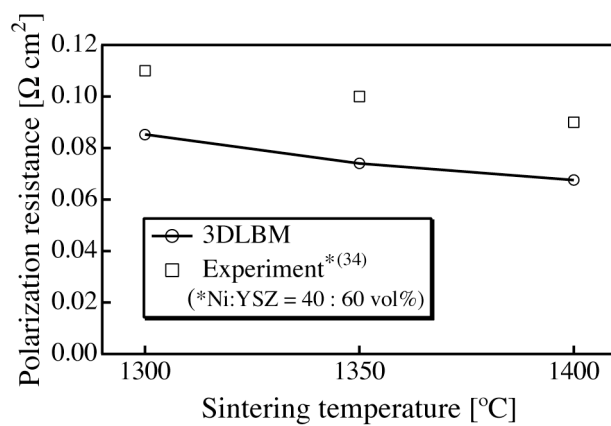


Fig. 11

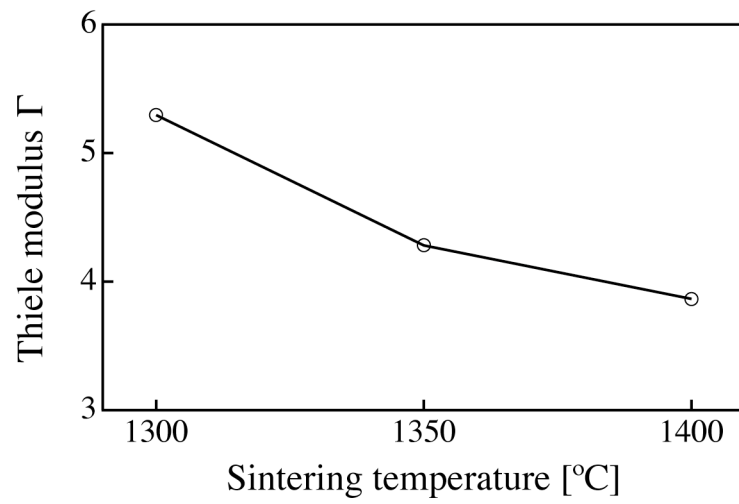


Fig. 12

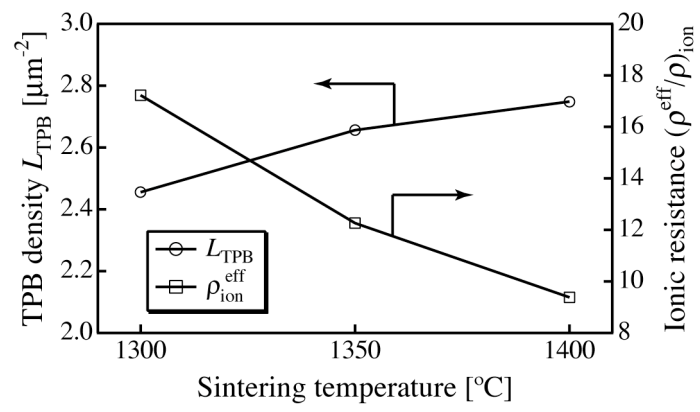


Fig. 13

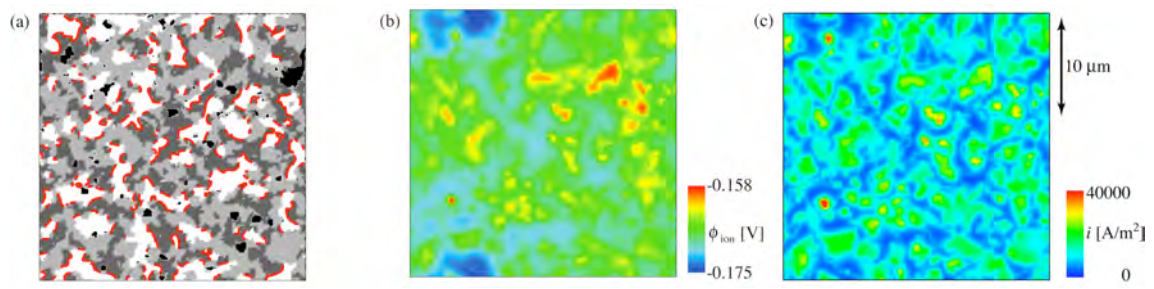


Fig. 14

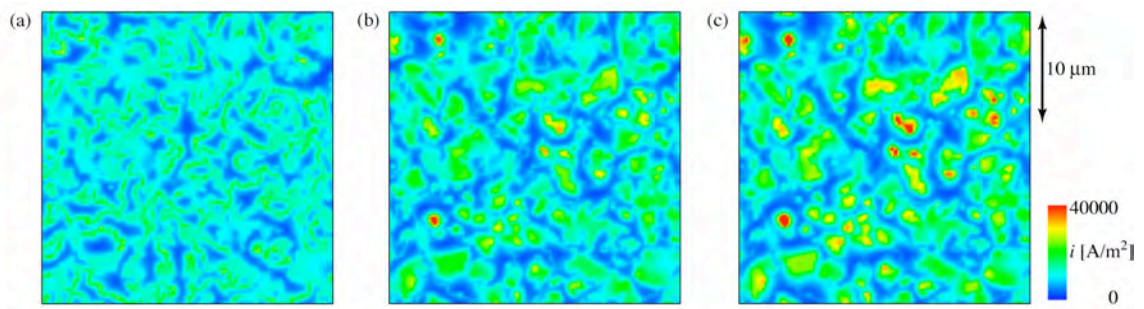


Fig. 15

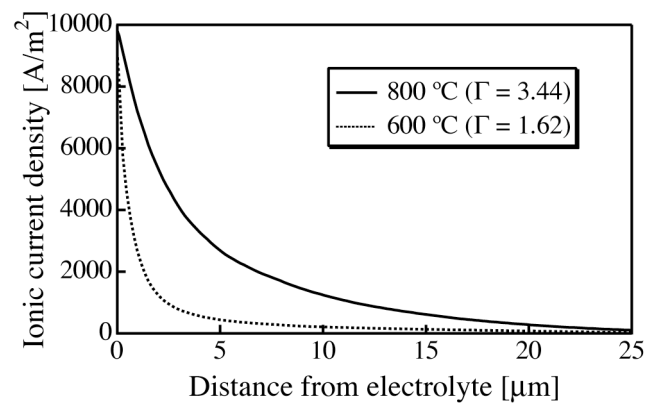


Fig. 16

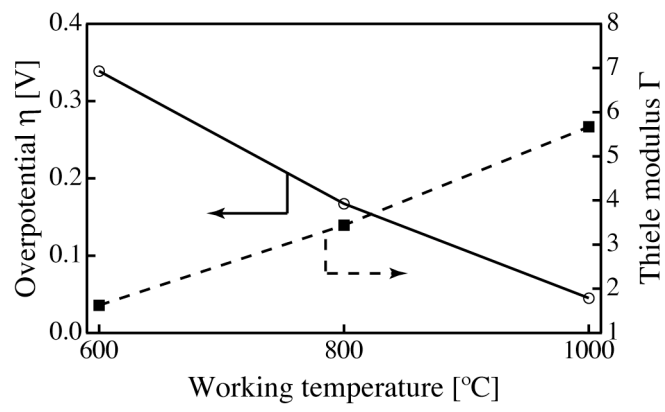


Fig.17